

# Stellar associations powering H II regions

## II. Escape fraction of ionizing photons

Fabian Scheuermann<sup>\*1</sup>, Kathryn Kreckel<sup>1</sup>, Jia Wei Teh<sup>2</sup>, Francesco Belfiore<sup>3,4</sup>, Brent Groves<sup>5,6</sup>, Ashley T. Barnes<sup>3</sup>, Médéric Boquien<sup>7</sup>, Mélanie Chevance<sup>2</sup>, Daniel A. Dale<sup>8</sup>, Oleg Egorov<sup>1</sup>, Simon C. O. Glover<sup>2</sup>, Kathryn Grasha<sup>9</sup>, Stephen Hannon<sup>10</sup>, Ralf S. Klessen<sup>2,11</sup>, Kirsten L. Larson<sup>12</sup>, Janice C. Lee<sup>13</sup>, Fu-Heng Liang<sup>1</sup>, Laura A. Lopez<sup>14</sup>, J. Eduardo Méndez-Delgado<sup>15</sup>, Justus Neumann<sup>10</sup>, Eve Ostriker<sup>16</sup>, Hsi-An Pan<sup>17</sup>, Lise Ramambason<sup>2</sup>, Francesco Santoro<sup>10</sup>, Eva Schinnerer<sup>10</sup>, David A. Thilker<sup>18</sup>, Qiushi Chris Tian<sup>18,19</sup>, Leonardo Úbeda<sup>13</sup>, Bradley C. Whitmore<sup>13</sup>, and Thomas G. Williams<sup>20</sup>

(Affiliations can be found after the references)

Received 10 August 2025 / Accepted 7 February 2026

### ABSTRACT

Newly formed stars have a profound impact on their environment by depositing energy and momentum into the surrounding gas. However, only a fraction of the stellar feedback is retained in the cloud and observational constraints are needed to further our understanding of this process. In a sample of 19 nearby galaxies, we match H II regions from PHANGS–MUSE to their ionizing stellar source from PHANGS–HST and measure the percentage of ionizing radiation that is leaking into the surrounding diffuse ionized gas (DIG). Based on a catalogue, where each H II region is powered by a single young and massive stellar association, we measure a photon escape fraction of  $f_{\text{esc}} = 82^{+12}_{-24}$  per cent. Comparable results are obtained when different procedures are used to match the ionized gas to its source. All samples we study contain a substantial fraction of objects (up to 20 per cent), where the stellar source is not sufficient to produce the H $\alpha$  flux observed from the nebula. Many of them are probably related to uncertain age estimates, but we also find numerous regions, where a significant fraction of the ionizing photon budget is contributed by stars that reside outside the boundaries of the H II region. This motivates the use of an alternative galaxy-wide approach, in which we include all H II regions and stellar sources, not just the ones that show a clear overlap. When summing up the ionization budget over entire galaxies, we measure slightly lower, but consistent values.

**Key words.** ISM: H II regions – Galaxies: ISM – Galaxies: star clusters: general – Galaxies: star formation

### 1. Introduction

Stellar feedback plays a crucial role in the evolution of the interstellar medium (ISM, Lopez et al. 2014; Klessen & Glover 2016; Krumholz et al. 2019). It shapes the surrounding gas, halts or triggers new star formation, and enriches the gas with metals. However, not all energy and momentum from the stellar feedback is deposited in the H II regions (Hanish et al. 2010). Turbulence and radiative feedback can fragment the cloud (Kakiichi & Gronke 2021), which opens up channels through which some radiation escapes, while part of the stellar feedback is absorbed by gas and dust. This is an important contribution to the diffuse ionized gas (DIG, Haffner et al. 2009).

A common way to constrain the leakage is by comparing the number of predicted ionizing photons emitted by individual stars or clusters,  $Q(\text{H}^0)$ , to the ionizing photon flux inferred from the observed H $\alpha$  luminosity of an associated H II region,  $Q_{\text{H}\alpha}$  (Niederhofer et al. 2016). This yields the escape fraction of ionizing photons which is usually defined as

$$f_{\text{esc}} = \frac{Q(\text{H}^0) - Q_{\text{H}\alpha}}{Q(\text{H}^0)}. \quad (1)$$

It is expected to evolve over time (Trebitsch et al. 2017) and depend on various local ISM conditions, such as gas density, metallicity and the star-gas geometry (Ramambason et al. 2022).

Therefore, having a large sample is necessary to marginalize over these variations, or explore trends.

For H II regions located within a massive galaxy, any escaping radiation is expected to primarily impact the surrounding galactic ISM and it is clear that within galaxies there are kpc-scale consequences of stellar feedback (Zurita et al. 2000; Belfiore et al. 2022). Connecting this feedback to the galactic escape fraction, which is vital to understanding cosmic reionization (Paardekooper et al. 2011; Mitra et al. 2013; Japelj et al. 2017; Kado-Fong et al. 2020; Ma et al. 2020; Ramambason et al. 2020; Wang et al. 2021; Chisholm et al. 2022; Saldana-Lopez et al. 2022; Flury et al. 2022a,b), is challenging.

Measurements of  $f_{\text{esc}}$  with various techniques have resulted in a wide range of estimates. One of the first attempts that applied a method similar to ours, i.e. analysing individual ionizing sources in nearby galaxies, was conducted by McLeod et al. (2020) for NGC 300. Because the galaxy is nearby (2.09 Mpc; Jacobs et al. 2009), they were able to use the Multi Unit Spectroscopic Explorer (MUSE) to identify individual O-stars as the source of the ionizing radiation. By matching them to two H II regions they measured an escape fraction of  $28 \pm 6$  per cent and  $51 \pm 1$  per cent respectively. Della Bruna et al. (2021) analysed 8 H II regions in NGC 7793 and found a value of  $f_{\text{esc}} = 67^{+8}_{-12}$  per cent. In Della Bruna et al. (2022), they applied their technique to M 83 and found 541 matches between H II regions and young star clusters. But only 13 per cent of them returned a positive  $f_{\text{esc}}$ , i.e. for most objects, the photons emitted by the

\* f.scheuermann@uni-heidelberg.de

stars were insufficient to explain the observed  $H\alpha$  emission. Recently, [Teh et al. \(2023\)](#) studied 42  $H\text{II}$  regions in NGC 628 and determined an escape fraction of  $9_{-6}^{+6}$  per cent.

Studies of even closer galaxies do not give more consistent results, although individual ionizing stars can be characterised and rich multi-wavelength constraints are available. [Pellegrini et al. \(2012\)](#) analysed 13  $H\text{II}$  regions in the Large Magellanic Cloud with known ionizing stars and infer typical escape fractions ranging from 30 to 60 per cent. However, in the extreme starburst region of the Tarantula Nebula, [Doran et al. \(2013\)](#) measured extremely low escape fractions of 5 to 10 per cent. The dwarf galaxies Holmberg I ([Egorov et al. 2018](#)) and Sextans A ([Gerasimov et al. 2022](#)) have well characterised O star populations and escape fractions of  $\sim 60$  per cent, but larger dwarf galaxy samples, where modelling included infrared constraints, typically return much lower 10 to 20 per cent escape fractions.

Within simulations, considerable progress has been made in recent years to include more realistic treatments of stellar feedback physics, but again a range of escape fractions are predicted as a function of both local conditions and time. Cloud-scale simulations with simplified feedback prescriptions (e.g. [Dale et al. 2012, 2013](#)) indicate that the escape fraction can vary widely over time as photoionization reshapes the cloud structure. Radiation-hydrodynamic models of turbulent clouds, some including magnetic fields ([Howard et al. 2017, 2018](#); [Kim et al. 2019, 2021b](#)), also find strongly time-dependent escape fractions that can briefly approach 100 per cent but average to only a few to ten per cent over a cloud’s lifetime. Semi-analytic feedback models ([Rahner et al. 2017](#)) predict similar trends, with escape fractions rising as feedback clears gas, while galaxy-scale simulations ([Tacchella et al. 2022](#)) infer global values of order a few per cent.

With the availability of large field-of-view integral field unit (IFU) spectroscopy instruments, like MUSE or the Spectromètre Imageur à Transformée de Fourier pour l’Etude en Long et en Large de raies d’Emission (SITELE), it is now possible to study the ionized gas using multiple optical emission line diagnostics, isolating individual  $H\text{II}$  regions while imaging the full star-forming disk for a large sample of nearby galaxies. In combination with space-based imaging (e.g. *Hubble Space Telescope*; *HST*) we are able to obtain an accurate census of the ionizing sources in galaxies beyond the Local Group. With its combination of MUSE and *HST* imaging, the Physics at High Angular resolution in Nearby Galaxies (PHANGS)<sup>1</sup> survey is ideally suited to the systematic study of star formation in nearby galaxies ([Leroy et al. 2021a,b](#); [Emsellem et al. 2022](#); [Lee et al. 2022, 2023](#)). In this work, we use the large sample of  $H\text{II}$  regions and stellar associations compiled in [Scheuermann et al. \(2023\)](#) to calculate  $f_{\text{esc}}$  and search for systematic variations with local physical conditions and star cluster properties.

This paper is organized as follows: in [Section 2](#) we present the catalogues and models that were used in this work. In [Section 3](#) we use these data to compute the escape fractions of the  $H\text{II}$  regions and discuss trends with physical properties. We conclude in [Section 4](#).

## 2. Data and models

Our sample consists of 19 PHANGS galaxies that were observed with both MUSE and *HST* and is listed in [Table 1](#). The matching of the nebulae and ionizing sources is described in detail in

<sup>1</sup> <https://www.phangs.org>

**Table 1.** Properties of the PHANGS galaxy sample.

Name	Distance (Mpc)	$N_{H\text{II}}$	$N_{\text{asc}}$	$N_{\text{clu}}$
IC 5332	$9.01 \pm 0.41$	608	397	193
NGC 0628	$9.84 \pm 0.63$	1651	1119	1365
NGC 1087	$15.85 \pm 2.24$	892	487	926
NGC 1300	$18.99 \pm 2.85$	1147	401	797
NGC 1365	$19.57 \pm 0.78$	445	489	833
NGC 1385	$17.22 \pm 2.58$	922	525	997
NGC 1433	$18.63 \pm 1.86$	729	494	390
NGC 1512	$18.83 \pm 1.88$	479	521	519
NGC 1566	$17.69 \pm 2.00$	1448	1582	2142
NGC 1672	$19.40 \pm 2.91$	1047	1247	1628
NGC 2835	$12.22 \pm 0.94$	777	649	728
NGC 3351	$9.96 \pm 0.33$	769	708	595
NGC 3627	$11.32 \pm 0.48$	1016	1325	2320
NGC 4254	$13.10 \pm 2.80$	2375	1661	3897
NGC 4303	$16.99 \pm 3.04$	1956	1736	3188
NGC 4321	$15.21 \pm 0.49$	984	1483	1921
NGC 4535	$15.77 \pm 0.37$	1168	469	567
NGC 5068	$5.20 \pm 0.21$	1405	715	1137
NGC 7496	$18.72 \pm 2.81$	523	265	385
Total		20 341	16 273	24 529

**Notes.** Distances compiled by [Anand et al. \(2021\)](#).  $N_{H\text{II}}$  is the number of  $H\text{II}$  regions,  $N_{\text{asc}}$  the number of stellar associations, and  $N_{\text{clu}}$  the number of clusters within the overlapping coverage of MUSE and *HST*.

[Scheuermann et al. \(2023\)](#), hereafter referred to as [Paper I](#). Below we provide a short summary of the individual data sets and how they are combined to form matched catalogues, as well as the stellar models that are used during the analysis.

### 2.1. MUSE HII regions

MUSE is a powerful optical IFU spectrograph that is mounted at the Very Large Telescope (VLT) in Chile ([Bacon et al. 2010](#)). It possesses a  $1 \times 1$  arcmin<sup>2</sup> field of view (FoV) and covers the wavelength range from 4800 to 9300 Å in the nominal mode. The PHANGS–MUSE survey (PI: Schinnerer) has produced wide-field mosaics of 19 nearby spiral galaxies. The analysis and the main data products are described in [Emsellem et al. \(2022\)](#). Among these are continuum subtracted emission-line maps, constructed by fitting single Gaussians to a set of bright emission lines (e.g.  $H\beta$ ,  $[\text{O III}]\lambda 5007$ ,  $H\alpha$ ,  $[\text{N II}]\lambda 6583$ ,  $[\text{S II}]\lambda 6717$ ,  $6731$ ,  $[\text{S III}]\lambda 9531$ ), which form the basis for our further analysis.

Based on the  $H\alpha$  morphologies, [Santoro et al. \(2022\)](#) and [Groves et al. \(2023\)](#) used this dataset to construct an  $H\text{II}$  region catalogue. In the first step, *HIIphot* ([Thilker et al. 2000](#)) was used to draw the boundaries of the emission line nebulae based on their  $H\alpha$  brightness. This initial catalogue is composed of 31 497 nebulae, but still contains other  $H\alpha$  bright objects like planetary nebulae (PNe) or supernova remnants (SNRs). They are removed by analysing diagnostic line ratios in the Baldwin–Phillips–Terlevich (BPT) diagrams ([Baldwin et al. 1981](#); [Veilleux & Osterbrock 1987](#)). We require regions to fall below the [Kauffmann et al. \(2003\)](#) diagnostic curve in the  $[\text{O III}]/H\beta$  versus  $[\text{N II}]/H\alpha$  diagrams, and below the [Kewley et al. \(2006\)](#) diagnostic curve in the  $[\text{O III}]/H\beta$  versus  $[\text{S II}]/H\alpha$  diagrams, with  $S/N > 5$  in all lines. Where  $[\text{O I}]$  is detected with  $S/N > 5$ ,

we further require that regions fall below the [Kewley et al. \(2006\)](#) diagnostic curve in the  $[\text{O I}]/\text{H}\beta$  versus  $[\text{S II}]/\text{H}\alpha$  diagram.

For this work, we only use the objects that fall inside the *HST* coverage, yielding 20 341  $\text{H II}$  regions in the final catalogue. In addition, properties like metallicity, ionization parameter and density are derived from the measured emission lines. For a full summary of the catalogue and the derived properties with detailed statistics, see also [Paper I](#).

We are primarily interested in the  $\text{H II}$  region  $\text{H}\alpha$  luminosity, which we want to compare to the predicted ionizing photon rate from the stars. The flux measurements for the nebulae are very precise, with a typical uncertainty of less than 1 per cent, but the uncertainties arising from the determination of the boundaries of the nebulae are not taken into account here. We need to correct the measured fluxes for extinction and for the Milky Way, we use the extinction curve from [O’Donnell \(1994\)](#),  $E(B - V)$  from [Schlafly & Finkbeiner \(2011\)](#) and  $R_V = 3.1$ . For the internal extinction, we adopt the same extinction curve and determine  $E(B - V)$  from the Balmer decrement, assuming  $\text{H}\alpha/\text{H}\beta = 2.86$ . To convert the fluxes to luminosities we use the distances listed in [Table 1](#).

In order to compare those values with the emission from the stars, we have to convert the  $\text{H}\alpha$  luminosity to the number of ionizing photons. This is commonly done with a conversion factor like the one by [Hummer & Storey \(1987\)](#). Assuming Case B recombination, an electron temperature of  $10^4$  K and a density of  $10^2 \text{ cm}^{-3}$  (well matched to our sample; [Barnes et al. 2021](#)) this yields

$$Q_{\text{H}\alpha} / \text{s}^{-1} = 7.31 \cdot 10^{11} L(\text{H}\alpha) / \text{erg s}^{-1}. \quad (2)$$

It should be noted that the temperatures observed in our  $\text{H II}$  regions can vary between 5000 and 10 000 K ([Kreckel et al. 2022](#)). We therefore run *INTRAT* by [Storey & Hummer \(1995\)](#) to compute the conversion factor for a number of temperatures and densities. A lower temperature of 5000 K would decrease the conversion factor by about 8 per cent, and imply that we slightly underestimate the number of ionizing photons (and hence overestimate the escape fraction) for some objects. An increase of the density to  $10^3 \text{ cm}^{-3}$  does not change the result by more than 0.3 per cent.

## 2.2. *HST* stellar associations and star clusters

All 19 galaxies are included in the PHANGS–*HST* survey ([Lee et al. 2022](#)), providing a sharp  $\sim 4$  pc view of ionizing stellar sources with coverage in five broadband filters: F275W (NUV), F336W (*U*), F438W (*B*), F555W (*V*), and F814 (*I*). From these images, we can identify and distinguish both compact, gravitationally bound star clusters, as well as physically larger, loosely bound stellar associations ([Elmegreen 2008](#); [Gouliermis 2018](#)). In [Paper I](#) we found that stellar associations provide a better one-to-one match to individual  $\text{H II}$  regions, however compact star clusters are easier to identify and model, and have been the focus of most previous studies constraining  $\text{H II}$  region escape fractions (e.g. [Della Bruna et al. 2021](#); [Teh et al. 2023](#)). Therefore, in this work we include both star clusters and stellar associations in our analysis, flexibly allowing  $\text{H II}$  regions to contain multiple ionizing sources.

The stellar association catalogue was created by [Larson et al. \(2023\)](#), and employs a watershed algorithm to join nearby young stars into a single object. Starting from either NUV or *V* tracer images, *DOLPHOT* is used to identify an initial set of point sources. This is then used to construct density maps, which are Gaussian smoothed to physical scales ranging from 8 to 64 pc. A watershed algorithm finally groups multiple peaks together in order

to form a single larger structure, or stellar association. Using the integrated fluxes of all stellar peaks within the association provides five band photometry of each catalogued object. As demonstrated in [Paper I](#), our analysis yields similar results when we use different scales and tracer bands, and we decide to use the 32 pc NUV catalogue for our analysis, as it has the largest overlap with our  $\text{H II}$  region catalogue. This catalogue contains 16 273 associations across 19 galaxies that fall inside the MUSE coverage. This number differs slightly from the one used in [Paper I](#). The previous association catalogue was an internal release and some associations in NGC 0628 lay outside the overlapping footprint of all five *HST* bands. This caused some issues with the SED fit and hence those few objects are now removed from the catalogue.

For the star clusters we use the catalogue created by [Thilker et al. \(2022\)](#) and [Maschmann et al. \(2024\)](#), which identifies marginally resolved sources in *HST* imaging and characterises them based on their morphology. The sources are detected with *DOLPHOT* and *DAOSTARFINDER* (v2.0, [Dolphin 2000](#); [Stetson 1987](#)) and classified into Classes 1, 2, 3, and 4 using machine learning models ([Wei et al. 2020](#); [Hannon et al. 2023](#)). Class 1 and 2 objects represent the compact clusters while Class 3 objects are often multi-peaked and are typically referred to as “compact associations” of stars. Class 4 objects are not considered to be star clusters, but instead are classified as artefacts like background galaxies or single stars, and are therefore excluded. As with the stellar associations, integrated fluxes are obtained for each object to provide five band photometry. The catalogue that we use contains 24 529 star clusters that fall inside the MUSE coverage (6593 of Class 1 or 2 and 17 936 of Class 3).

For both the stellar association and compact star cluster catalogues, the age, mass, and reddening were derived by fitting the *HST* five band spectral energy distribution (SED) as described in [Turner et al. \(2021\)](#). To do this, Code Investigating GALaxy Emission (*CIGALE*) by [Boquien et al. \(2019\)](#) was used with theoretical models of a single stellar population by [Bruzual & Charlot \(2003\)](#), a metallicity of  $Z = 0.02$ , and assuming a fully-sampled [Chabrier \(2003\)](#) initial mass function (IMF). Since the publication of [Paper I](#), the cluster catalogue was updated by [Thilker et al. \(2025\)](#). However, they are broadly consistent and the changes do not alter our results, so for reproducibility we carry out our analysis on the catalogue presented in [Paper I](#).

We note a few caveats on the use of these catalogues to study the youngest stellar populations. A limited colour-space is used to derive the stellar properties, with five *HST* bands used to fit three stellar properties (mass, age, and reddening). While this will be refined in the near future with the inclusion of additional *JWST* bands ([Lee et al. 2023](#)), the lack of suitable FUV coverage still presents a problem, especially for the youngest clusters. While the galaxies were observed with *GALEX* ([Martin et al. 2005](#)) and *AstroSat* ([Hassani et al. 2024](#)), the resolution of those instruments are not sufficient for the analysis. Another issue that we cannot address with our current data is the contribution of Wolf-Rayet stars ([Crowther 2007](#)) or other massive single stars ([Zastrow et al. 2013](#)) to the ionizing photon output.

## 2.3. Calculating the number of ionizing photons

What is missing in the published catalogues is the number of ionizing photons  $Q(\text{H}^0)$  that is emitted by the stars. This number can depend on a variety of assumptions, such as the adopted stellar atmosphere model ([Simón-Díaz & Stasińska 2008](#)), stellar rotation ([Levesque et al. 2012](#)), and binarity ([Lecroq et al. 2024](#)). In this section we use a number of different codes to compute

$Q(H^0)$  as a way of understanding the systematics that go into this calculation.

Generally, the models take a certain IMF to create a grid of stars and then compute the ionizing photon flux as a function of age, based on different stellar models and atmospheres. If the IMF is fully sampled, the output scales linearly with mass. This should be treated with caution, as this is certainly not the case for lower mass clusters (Cerviño & Luridiana 2006). We try to circumvent this problem by applying certain mass cuts, as discussed in Section 2.4. To propagate the uncertainties from the ages, we assume a Gaussian age distribution that is clipped at 1 Myr and draw a random sample for which we then compute  $Q(H^0)$ . Since the flux is expected to scale linearly with mass (for a fully-sampled IMF), error propagation is straightforward. The uncertainty of the distance affects the  $H\alpha$  luminosity and the derived cluster mass in the same way and is therefore not included.

For the comparison, we consider results from CIGALE, STARBURST99 (the models without rotation SB99 v00 and those with rotation SB99 v40), and the binary model from the Binary Population and Spectral Synthesis code (BPASS). An overview of the details and the age-dependency of different models is shown in Section A. Another popular model is Stochastically Lighting Up Galaxies (SLUG, da Silva et al. 2012), but instead of discrete values, it treats the individual properties as probability distributions. This makes it difficult to include here and we refer to Section B for some simplistic comparisons of our results with what is modelled by SLUG.

### 2.3.1. BC03

As previously stated, CIGALE (Boquien et al. 2019) was used to fit the SED and derive stellar properties. Therefore the self-consistent approach is to also use the ionizing photon flux that is computed by this code. The catalogues published by Thilker et al. (2022) and Larson et al. (2023) do not contain this quantity, so we run CIGALE with the same input parameters in savefluxes mode to compute the ionizing photon flux as a function of age. We then use the previously fitted ages and masses of each stellar cluster and association to interpolate their value of  $Q(H^0)$ . The stellar models from Bruzual & Charlot (2003) are used, together with an IMF from Chabrier (2003).

### 2.3.2. SB99

Another popular stellar population synthesis model is STARBURST99 (Leitherer et al. 1999, 2010, 2014; Vázquez & Leitherer 2005). As input parameters, we select a single burst of star formation that follows a fully-sampled Kroupa (2001) IMF with the Geneva stellar models at solar metallicity (Ekström et al. 2012) and stellar atmospheres from Lejeune et al. (1997). The remaining parameters are left at their default values. After that we use the stellar ages and masses again to interpolate the output to the values in our sample. While it represents more of an extreme case, we also consider a model with rotating stars, spinning at 40 per cent break-up velocity, as a limiting case.

### 2.3.3. BPASS

Most models track single star evolution, but many stars form in binaries, which impacts their evolution (Sana et al. 2012). Fortunately for us, the difference in ionizing photons is expected to only become significant after 8 Myr (Lecroq et al. 2024), and hence this should not be an issue for our purposes. In order to get

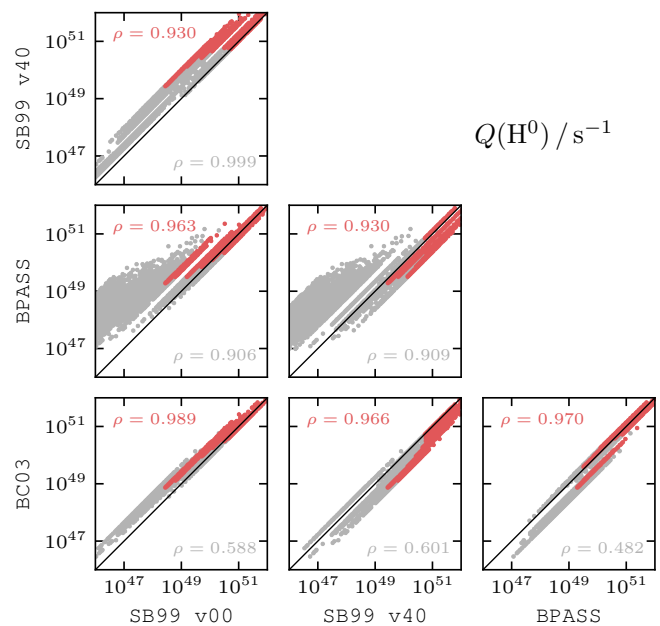


**Fig. 1.** Comparison between different population synthesis models. We use a sample with random ages and masses and compute the ionizing photon flux  $Q(H^0)$  with BC03, SB99, and BPASS. The grey points are the full sample and the red points show a young and massive subsample (age  $\leq 8$  Myr and mass  $> 10^4 M_\odot$ ). The Spearman correlation coefficient  $\rho$  indicates good agreement between the different models across the robust subsamples, and all of the correlations are statistically significant with  $p$ -values  $< 0.05$ .

a rough estimate on the impact binarity might have on  $Q(H^0)$ , we include BPASS by Eldridge & Stanway (2009) in our comparison. We employ the fiducial model for binaries from version 2.1 (Eldridge et al. 2017) with a Kroupa IMF (Kroupa 2001) and an upper mass limit of  $300 M_\odot$  at solar metallicity.

### 2.3.4. Comparison between the different models

To gauge the variations between the different models introduced in the previous sections, we compare the fluxes they predict for a random sample. For this, we create 10 000 clusters with random ages and masses, selected to be representative of the objects in our real sample. This is just meant to provide some order of magnitude understanding of the impact different processes have on our result.

The comparison of the predicted ionizing photon flux  $Q(H^0)$  is shown as a corner plot in Figure 1. Overall we find decent agreement between most models, but there are a few noticeable, systematic differences. The models with rotation predict higher ionizing photon fluxes, as expected from the study of Levesque et al. (2012). As for BPASS, there are two distinct branches: during the first few Myr the agreement is good, but around 6 Myr the difference between single stars and binaries becomes relevant.

While the models can differ significantly from one another, those differences affect mostly a specific part of the samples, like older or low-mass clusters. For the objects that are young and massive, the differences are much smaller and all models return similar values. For the remainder of the paper, we use the STARBURST99 model without rotation as our fiducial model.

## 2.4. Matched catalogues

Based on the one catalogue for the H II regions and the two for the stars (clusters and associations), it is possible to define different matched catalogues. Here we describe the different samples that are used in this paper. Figure 2 illustrates examples for possible overlaps and Table 2 provides an overview of the different samples and their sizes.

### 2.4.1. one-to-one sample

The ideal scenario is a single H II region that is powered by a single stellar population, as this enables us to study trends of the escape fraction with different nebula and stellar properties. This is the case for the catalogue that was published in Paper I. It consists of H II regions and stellar associations that have a clear one-to-one match and contains 4169 objects in the full sample. This includes 20.5 per cent of all H II regions and 25.6 per cent of the associations.

For lower mass associations, the presence or absence of individual massive stars can have a significant impact on the measured fluxes (Fouesneau & Lançon 2010; Fouesneau et al. 2012; Hannon et al. 2019). To alleviate stochastic sampling effects of the IMF, we also define a robust one-to-one subsample, consisting of objects that are more massive than  $10^4 M_{\odot}$ , with ages of 8 Myr or less, and fully contained within the nebulae. This leaves us with 474 objects and constitutes our fiducial sample that we will use as a reference throughout the paper. They are spread across all galaxies apart from NGC 5068 (the lowest mass galaxy in our sample). Panel a) in Figure 2 shows an example for such an object.

### 2.4.2. extended sample

As laid out in Paper I, a considerable number of our detected H II regions (14.7 per cent) overlap with more than one association. In this regard, we find 2981 H II regions that contain 8871 stellar associations, but some of the associations overlap with another H II region, making it difficult to map their ionizing photon flux to the correct nebula. We therefore limit ourselves to the 966 H II regions where the associations do not overlap with another H II region (a total of 2248 associations). Over three-quarters of them contain two associations and only a single one contains more than six associations. We refer to this sample as the extended sample and panel b) and c) in Figure 2 show postage stamp cutouts for this sample.

Again we aim to define a robust subsample, however, in this case the definition is not so straightforward. We require that at least one association is young and massive ( $> 10^4 M_{\odot}$  and  $\leq 8$  Myr), and there are 707 of them in the initial catalogue. As for the overlap, we are less concerned about the old or light associations, but if a young and massive one only partially overlaps, we remove the object. This leaves us with 291 objects for our robust extended subsample. In comparison to the one-to-one sample, the H II regions in the extended catalogue are brighter in H  $\alpha$  by a factor of 5.

### 2.4.3. complexes sample

As alluded to in Section 2.1, difficulties in drawing the boundaries of the H II regions can lead to large uncertainties for the measured fluxes. This is particularly problematic for the 34 per cent of our H II regions that touch another ionized nebula.

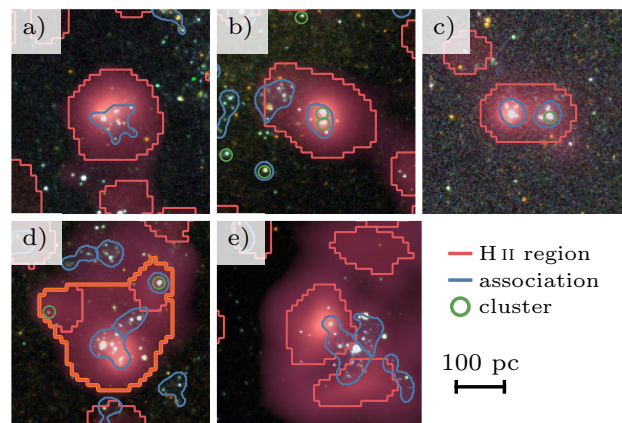


**Fig. 2.** Examples for the overlap between H II regions and their ionizing sources. Each cutout shows three-colour composite images, based on the five available *HST* bands, overlaid with the H  $\alpha$  line emission of MUSE in red. a) an H II region with a fully contained association; b) an H II region with a fully and a partially contained association and two compact clusters; c) an H II region with two fully contained associations and a compact cluster; d) multiple H II regions that form a single H II region complex with multiple associations and clusters; e) an association that overlaps with two H II regions.

For this sample, we group bordering nebulae together and call them a complex. We find 9434 nebulae in 3019 complexes, but many of them contain ionized nebulae inconsistent with photoionization (e.g. SNRs or PNe), indicating that other processes may contribute to the H  $\alpha$  emission. There are also complexes that do not contain an ionizing source while for some the ionizing source is shared with another complex (two complexes that do not touch, but share an association that overlaps with both as shown in panel e) of Figure 2). Excluding all of them leaves 1124 complexes in our sample that contain 3722 H II regions and 3923 associations. An example for such an object can be seen in panel d) of Figure 2.

For the robust subsample, we apply the same criteria as for the robust extended sample, i.e. at least one fully contained young and massive association and no partially overlapping young and massive ones. This leaves 317 objects in the robust complexes subsample.

### 2.4.4. cluster sample

In order to directly compare our results with existing studies that focused on star clusters instead of stellar associations (e.g. Della Bruna et al. 2021; Teh et al. 2023), we also construct a sample focused on the overlap of H II regions and star clusters. We use the Class 1, 2, and 3 clusters from Thilker et al. (2022) and find 22 632 clusters that overlap with 8905 H II regions. Similar to the extended sample, having multiple clusters inside one H II region is not an issue, and this constitutes our cluster sample. We also apply the same mass and age restrictions for the robust subsample (the overlap criterion does not apply as the clusters are treated as point sources), and find 2223 objects in the robust cluster subsample.

## 3. Escape fractions

As is evident from the previous section, there are many assumptions involved in the calculation, but the choice of the stellar pop-

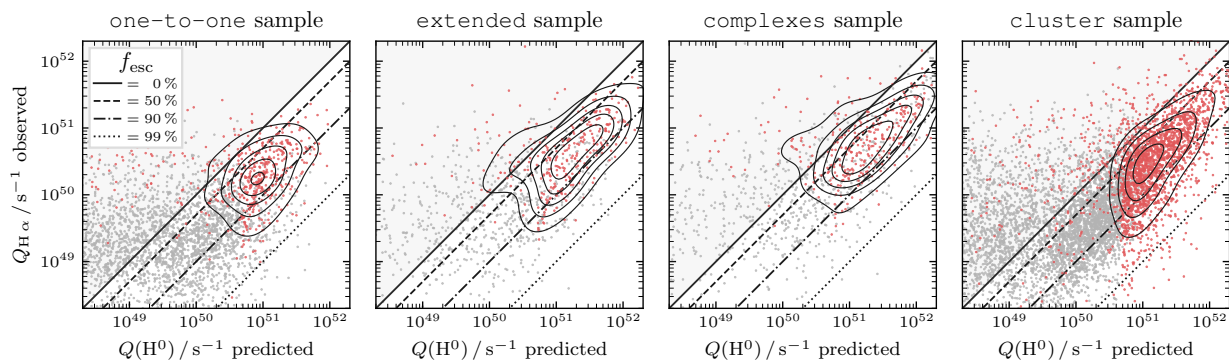


**Fig. 3.** We compare the predicted ionizing photon flux  $Q(H^0)$  to the observed values from the H II region  $Q_{H\alpha}$ . The full samples are shown in grey and the robust subsamples in red. The contours indicate the distribution of the robust sample and the diagonal lines correspond to different escape fractions.

**Table 2.** The matched samples we define for this paper.

Name	Sample size	Description
one-to-one	4169 (474)	H II regions with a one-to-one match to a stellar association (from Paper I).
extended	966 (291)	H II regions that contain multiple stellar associations.
complexes	1124 (317)	Multiple H II regions that form a larger complex and contain one or more associations.
cluster	8905 (2223)	H II regions that contain one or more compact clusters.

**Notes.** The size of the robust subsamples is in parenthesis.

ulation model should only slightly alter the value of  $Q(H^0)$  for the robust subsamples. Here we shift our focus to the different samples that were defined. By combining the values from the H II regions to those from the stellar catalogues we estimate the percentage of leaking radiation.

### 3.1. Ionizing photon fluxes for different samples

We start by taking the samples defined in Section 2.4 and plot their observed ionizing photon flux from the H II regions,  $Q_{H\alpha}$ , against the one predicted from the stars,  $Q(H^0)$ . The result is shown in Figure 3 and the robust subsamples are marked in red.

Looking on the one-to-one sample, we find that for more than half of the full sample, the ionizing photon production rate from the associations is not sufficient to explain the observed H  $\alpha$  flux. However, most of those objects are either low-mass or only partially overlap. Focusing only on the previously defined robust one-to-one subsample, we find that 80 per cent of the H II regions can be ionized by their associated stars. The stellar association catalogues created at different physical scales (16 pc or 64 pc, see also Paper I) provide similar results.

For the other samples, we find similar trends, emphasizing the importance of selecting robust subsamples. It also becomes clear that the different catalogues probe different regimes in terms of the intensity of the ionizing photon flux. Unsurpris-

ingly, the extended sample and the complexes sample have ionizing photon fluxes that are on average more than four times as large as the one-to-one sample.

### 3.2. Distribution of the escape fraction

With  $Q(H^0)$  from the stars and  $Q_{H\alpha}$  from the H II regions, we use Equation (1) to compute the percentage of escaping ionizing radiation. As already obvious from Figure 3, for a substantial number of objects, the ionizing photon flux from the stars is not sufficient to ionize their matched H II region. As a result, some objects have a negative escape fraction, which makes it somewhat ambiguous how to determine a representative escape fraction for the sample as a whole. Excluding all regions with negative  $f_{\text{esc}}$  leads to a higher average, while including values that are clearly unphysical also does not make sense. Our approach is a compromise to account for objects that have a positive escape fraction within their uncertainties. We assume that the escape fraction for each object follows a normal distribution and sum up the individual distributions

$$p(x) = \sum_{i=1}^n \frac{1}{\sqrt{2\pi} \sigma_{f_{\text{esc},i}}} \exp\left(-\frac{(\mu_{f_{\text{esc},i}} - x)^2}{2\sigma_{f_{\text{esc},i}}^2}\right). \quad (3)$$

We then compute the median (50th percentile) and the  $1\sigma$  interval (16th and 84th percentile) in the range of valid values (0 to 100 per cent). The results are shown as histograms in Figure 4 and the majority has an escape fraction larger than 50 per cent. In the case of the robust subsamples, independent of the source of ionization, we measure similar medians, ranging from 76 to 82 per cent. The medians of the full samples are always within a few per cent of those values. The number of objects with negative escape fractions varies between 12 and 19 per cent and they are grouped together in the left bar.

### 3.3. What about negative escape fractions?

There is a considerable number of objects with a negative escape fraction, so here we take a closer look at what may cause this. The objects with a negative escape fraction in the robust one-to-one subsample are consistent with  $f_{\text{esc}} = 0$  within their uncertainties. Looking at the contributors to the absolute uncertainty, the dominant factor is the age, followed slightly behind by the mass while the error on the H  $\alpha$  flux is mostly negligible. It is therefore not surprising that most objects with a negative escape fraction are 4 Myr or older and have a median uncertainty

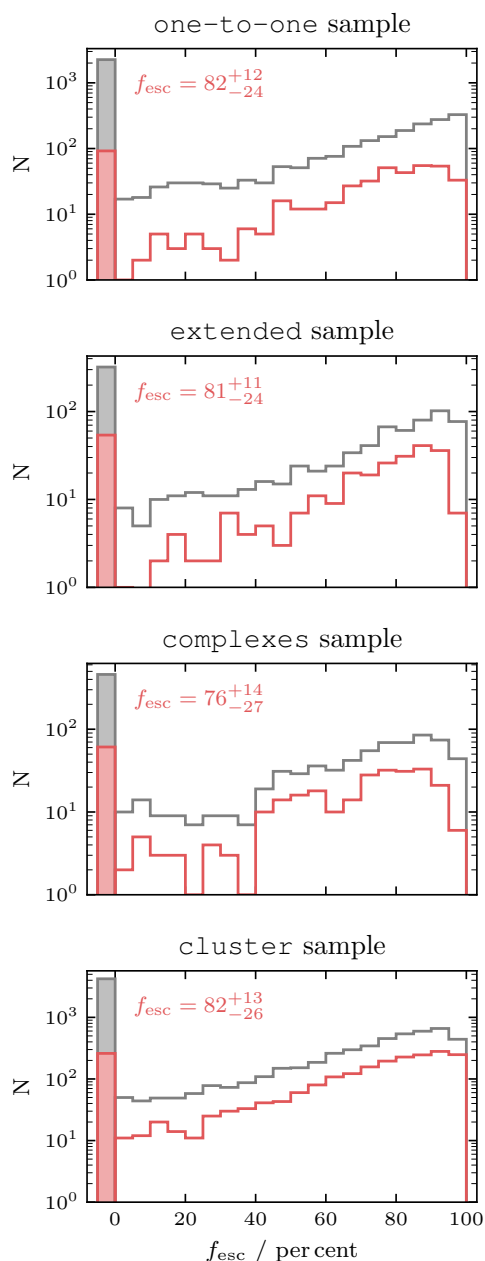


**Fig. 4.** Histograms of the observed escape fractions for the different samples. All regions with negative escape fractions are grouped together in the shaded left bar. The full sample is shown in gray and the robust subsample and its median in red.

of 2 Myr which makes them particularly susceptible that their predicted flux is wrong. An overestimation of the age could account for an underestimation of  $Q(\text{H}^0)$  and hence resolve most of the negative escape fractions.

Another possibility is that we are missing some ionizing sources all together. To explore this, we visually inspect the NUV images of the 92 objects with negative escape fraction and look for missed peaks inside the H II regions. Only about 10 per cent of them show peaks that were not included by the source detection of the associations.

Along these lines, the cloud might also be ionized by stars that fall outside of the H II region. To follow up on this point, for each H II region, we compile a list of associations that are within 10 arcsec (this corresponds to 250 to 950 pc, measured

from boundary to boundary). We then take the flux of each of those nearby associations (excluding associations that are fully contained in another H II region) and scale the estimated ionizing photons that could be absorbed by the H II region, assuming the flux is emitted isotropically. For each H II region, we compare the ionizing photon flux that originates from external sources to the one coming from overlapping sources. The result is shown in Figure 5. We find that in the subsample with negative escape fraction the estimated contribution from external ionizing photons is about a factor of 10 more than the internal contribution, which is more than a factor 100 larger than what is found in the subsample with positive escape fraction. However, even after accounting for these external contributions, the majority of the objects with negative escape fraction remain negative. Nevertheless, it shows that the escape fraction is underestimated if external sources are not taken into account.

So far we have mainly focused on the stellar side, but the  $Q_{\text{H}\alpha}$  estimated from the H II regions is also subject to uncertainties. Given that the H $\alpha$  fluxes are directly measured and have a high S/N, the stated errors are significantly smaller for  $Q_{\text{H}\alpha}$  than for  $Q(\text{H}^0)$ , but this does not include uncertainties due to choices like where we define the boundaries of the regions. Even a small change in the size can significantly alter the measured flux. This is especially true for closely clustered and unresolved H II regions, where we might attribute the measured flux to a neighbouring object. Increasing or decreasing the boundary by just one pixel radially (this corresponds to 5 to 19 pc, depending on the distance to the galaxy) will alter the measured flux on average by  $\pm 40$  per cent for the full H II regions sample, by  $\pm 30$  per cent for the matched objects, and by  $\pm 18$  per cent for the robust subsample. However, the flux measured from the H II regions is only roughly a fifth of the one predicted from the stars, so although the uncertainty itself is high, it typically changes the escape fraction by less than 5 per cent.

In addition, in particular for faint H II regions, the DIG might contribute a majority of H $\alpha$  emission, though our brighter robust sample should only be impacted at a  $\sim 20$  per cent level (Belfiore et al. 2022; Congiu et al. 2023).

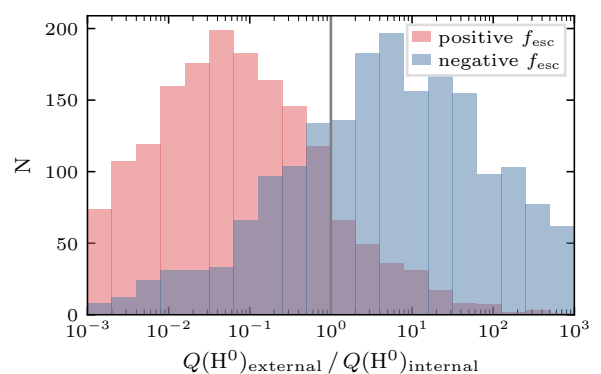


**Fig. 5.** Contribution of external ionizing sources. For H II regions with negative escape fractions, the average contribution from nearby associations, not overlapping with the nebula, is far greater than for those with positive escape fractions.

### 3.4. Photoionization budget of entire galaxies

As we previously saw, it is difficult to correctly assign each H II region to their source of ionizing radiation. A careful selection is required in order to include all real sources, while excluding any

**Table 3.** Ionizing photon budget for entire galaxies.

Name	H II regions	Stellar associations		Star cluster	
	$\log(Q_{\text{H}\alpha} / \text{s}^{-1})$	$\log(Q(\text{H}^0) / \text{s}^{-1})$	$f_{\text{esc}} / \text{per cent}$	$\log(Q(\text{H}^0) / \text{s}^{-1})$	$f_{\text{esc}} / \text{per cent}$
IC 5332	51.56 ± 0.06	52.38 ± 0.04	84.9 ± 2.5	52.13 ± 0.36	73.0 ± 22.5
NGC 0628	52.50 ± 0.04	53.29 ± 0.01	83.5 ± 1.6	53.05 ± 0.58	71.7 ± 37.7
NGC 1087	53.11 ± 0.06	53.65 ± 0.04	71.4 ± 4.6	53.55 ± 0.15	63.7 ± 13.0
NGC 1300	52.70 ± 0.04	52.97 ± 0.06	45.5 ± 9.2	53.25 ± 1.98	71.5 ± 130.1
NGC 1365	53.15 ± 0.14	53.43 ± 0.06	47.5 ± 18.4	53.48 ± 0.57	52.8 ± 64.0
NGC 1385	53.34 ± 0.05	53.70 ± 0.04	56.3 ± 6.4	53.61 ± 0.04	46.8 ± 7.3
NGC 1433	52.26 ± 0.04	52.71 ± 0.02	64.0 ± 4.0	53.00 ± 0.14	81.4 ± 7.1
NGC 1512	52.29 ± 0.05	52.62 ± 0.03	53.2 ± 6.3	53.59 ± 0.17	95.0 ± 5.6
NGC 1566	53.44 ± 0.06	53.99 ± 0.02	71.7 ± 4.0	53.85 ± 0.20	61.4 ± 17.8
NGC 1672	53.26 ± 0.05	53.72 ± 0.02	65.5 ± 4.1	53.67 ± 0.42	61.1 ± 37.4
NGC 2835	52.56 ± 0.05	53.14 ± 0.03	74.1 ± 3.6	53.18 ± 0.44	76.1 ± 24.2
NGC 3351	51.99 ± 0.04	52.95 ± 0.05	89.0 ± 1.6	52.72 ± 0.19	81.5 ± 8.3
NGC 3627	53.42 ± 0.04	53.75 ± 0.05	53.9 ± 7.0	53.81 ± 0.29	59.7 ± 27.5
NGC 4254	53.47 ± 0.02	54.06 ± 0.03	74.1 ± 2.2	54.10 ± 0.04	76.6 ± 2.6
NGC 4303	53.60 ± 0.03	54.13 ± 0.02	70.0 ± 2.6	54.17 ± 0.07	72.9 ± 4.9
NGC 4321	53.05 ± 0.04	53.77 ± 0.02	80.8 ± 2.1	53.69 ± 0.05	76.9 ± 3.3
NGC 4535	52.73 ± 0.04	53.27 ± 0.05	71.0 ± 4.2	53.34 ± 0.16	75.4 ± 9.6
NGC 5068	52.20 ± 0.05	52.63 ± 0.04	62.9 ± 5.6	52.67 ± 0.12	65.7 ± 10.8
NGC 7496	52.62 ± 0.06	53.23 ± 0.03	75.8 ± 3.9	53.20 ± 0.05	74.0 ± 4.7
Total	54.36 ± 0.02	54.87 ± 0.01	68.9 ± 1.3	54.88 ± 0.07	69.6 ± 5.0

**Notes.** We use the H II regions from [Santoro et al. \(2022\)](#) and [Groves et al. \(2023\)](#) and either the stellar associations (32 pc, NUV) from [Larson et al. \(2023\)](#), or the compact star clusters from [Thilker et al. \(2022\)](#).

false ones. Another approach would be to simply consider all objects together in order to avoid problems with the matching. And as we saw in [Figure 5](#), sources outside the H II region can have a significant contribution to the ionizing photon budget as well. We therefore perform this analysis on all H II regions and associations in the overlapping coverage of MUSE and *HST*. Since we have no way of excluding H II regions that are ionized by older or low-mass associations, this analysis also has to include all associations and not just the robust subsample. One potentially problematic area are the galactic centres, as some galaxies possess active nuclei. We therefore use the environment masks from [Querejeta et al. \(2021\)](#) to mask out the centres of the galaxies (this eliminates 286 H II regions and 690 associations from our sample).

We sum up the observed ionizing photon flux across all H II regions that fall inside the *HST* coverage, and measure  $Q_{\text{H}\alpha} = 2.3 \cdot 10^{54} \text{ s}^{-1}$  across all galaxies. We then sum up the predicted ionizing photon flux from all associations inside the MUSE coverage, and find  $Q(\text{H}^0) = 7.2 \cdot 10^{54} \text{ s}^{-1}$ , yielding an escape fraction of  $f_{\text{esc}} = 68.9 \pm 1.3$  per cent. Similarly, we can sum up the flux from all star clusters, resulting in a value of  $Q(\text{H}^0) = 7.4 \cdot 10^{54} \text{ s}^{-1}$  and an escape fraction of  $f_{\text{esc}} = 69.6 \pm 5.0$  per cent. The values for the individual galaxies are listed in [Table 3](#) and displayed in [Figure 6](#).

From this approach, the upper end of the luminosity function should be fully sampled for both the associations and H II regions, but there are differences in the sensitivity at the lower end. When looking at the cumulative luminosity function (see also [Section C](#) for more details), we see that it is dominated by the brightest objects. H II regions fainter than  $10^{38} \text{ erg s}^{-1}$  contain less than 10 per cent of the total ionizing photon flux (this is already ten times brighter than the completeness limit estimated by [Santoro et al. 2022](#)). This means that completeness should

not be an issue for the H II regions. As for the stars, they are even more dominated by the upper end of the luminosity function.

Other minor adjustments to our approach have only a negligible impact on our global result. If we have excluded some real H II regions with the BPT cuts, thereby artificially reducing the observed ionizing photon flux and increasing the escape fraction, we estimate that these only contribute around  $\sim 10$  per cent to the total  $\text{H}\alpha$  flux in all nebulae. This would only decrease the resulting escape fraction by a few per cent. There are also some compact clusters that are not contained inside an association. Including them in our analysis raises the predicted ionizing photon flux only slightly and the escape fraction only increases by  $\sim 3$  per cent.

Overall, both our global approach and our resolved approach return comparatively high values of 70 per cent and above, providing confidence in our overall result for this large statistical sample of stellar sources and H II regions.

### 3.5. Trends with nebulae properties

The escape fraction is expected to change as the cloud evolves ([Dayal & Ferrara 2018](#)) and as a function of local conditions. For example, one might expect higher  $f_{\text{esc}}$  in lower density environments or older H II regions, as the gas is already partially cleared. In [Figure 7](#) we present trends with selected properties. For this analysis we use the robust one-to-one subsample. In general, the large scatter in  $f_{\text{esc}}$  makes it challenging to identify strong correlations.

Contrary to our expectations, we find that H II regions containing younger associations are leakier (similar to the results reported by [Teh et al. 2023](#)). As a function of the stellar mass of the associations, the scatter is too large to identify any trends. In terms of the dust reddening, as traced by the Balmer decre-

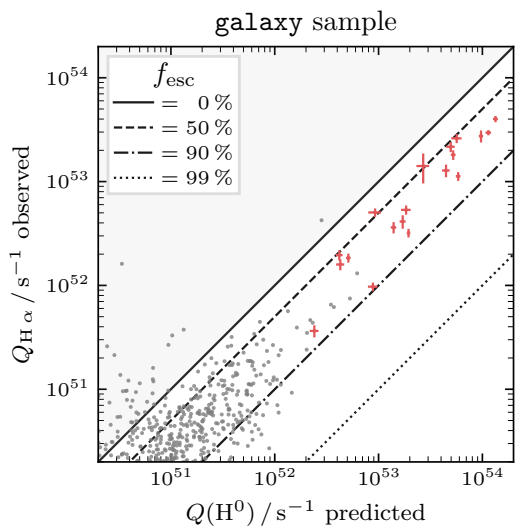


**Fig. 6.** Same as Figure 3 but with the ionizing photon budget for entire galaxies. The values for the galaxies are listed in Table 3 and include all H II regions and stellar associations in the overlapping coverage. For reference, the values of individual objects from the robust one-to-one and robust extended sample are plotted as grey dots.

ment, we observe an anti-correlation, consistent with the picture that a deeply embedded cloud leaks less radiation than a more permeable one. However, using the stellar  $E(B - V)$  we do not find a strong correlation. For the ionization parameter,  $\log q$ , and the local metallicity offset,  $\Delta(O/H)$ , we do not find any correlation. Lastly, for the individual H II regions, we look at the H  $\alpha$  luminosity and find an anti-correlation with the escape fraction, similar to Teh et al. (2023).

Based on our global measurements of  $f_{\text{esc}}$ , we also search for galaxy-wide trends. The escaping photons are thought to ionize the DIG and hence we expect a positive correlation. However, we see no trend between our observed  $f_{\text{esc}}$  and the fraction of the DIG  $f_{\text{DIG}}$  measured by Belfiore et al. (2022), whereby our values are also generally larger. Another property is the global metallicity  $12 + \log O/H$  (taken from Kreckel et al. 2020), but here too we see no dependency.

Finally, we look at the variations between different galactic environments within each galaxy, considering separately the bar, interbar, interarm, and spiral arm environments. While overall they are very similar, with medians ranging from 75 to 83 per cent, the H II regions in the bar have slightly lower escape fractions.

### 3.6. Comparison with existing studies

The large sample of H II regions and stellar sources that we use to measure the escape fraction results in a wide span of values. Looking at their distribution, it becomes evident that it is deceptive to quote a single value. The values published in the literature reinforce this as they also cover a wide range, depending on the conditions of the studied objects and the techniques used for the analysis.

We therefore focus our comparison on similar studies that also match observed H II regions to their stellar counterparts in nearby galaxies. Most of our measurements of the escape fraction exceeds 60 per cent, which itself falls at the upper end of values present in the literature (9 to 67 per cent) of comparable studies like McLeod et al. (2020) or Della Bruna et al. (2021). Even

for independent calculations done in exactly the same galaxy (NGC 0628 by Teh et al. 2023; see Appendix B), our approach returns much larger values for  $f_{\text{esc}}$ . While it is clear that specific modelling and measurement approaches can introduce large scatter, it is not obvious that there is any clear systematic difference from our approach compared to what has been previously done. We aim to highlight here that these modelling uncertainties remain dominant while attempting to quantitatively constrain the escape fraction and below we emphasize a number of issues that stand out.

The large size of our sample prompted us to introduce certain cuts to define a robust subsample where we remove objects we deem unreliable. The stellar component must be fully contained within the H II region, its mass must be larger than  $10^4 M_{\odot}$  to ensure that the IMF is fully sampled, and its age must be  $\leq 8$  Myr because the ionized cloud should not exist much longer than a few Myr (Hollyhead et al. 2015; Kim et al. 2021a; Hannon et al. 2022). This procedure is certainly more objective than picking the objects by hand, but it might still be biased towards certain physical parameters. Partly due to this selection, the regions in our sample are rather young with a median age of 2 Myr. Nevertheless, the age distribution seems physically reasonable, as according to Kim et al. (2023), 50 per cent of the LyC photons are already emitted by this age. Around this age, the ionizing photon flux is strongly dependent on the age and hence even a small uncertainty of only 1 Myr can cut the value for  $Q(H^0)$  in half. This is also reflected in the propagated error of  $f_{\text{esc}}$ , for which this is the biggest contributor.

Then there are also other issues whose uncertainties are difficult to incorporate. As mentioned in Section 2.1, a small change to the size of a region can alter the flux considerably and this is not accounted for in the stated error. When manually inspecting some of the outliers, it becomes clear that especially the larger H II regions are often complicated complexes that are difficult to segment into physically meaningful pieces. Furthermore, we do not consider external sources, which can have a major impact on small H II regions as shown in Section 3.3.

One aspect that we have not yet addressed is the impact of dust. This is a complex issue, and while some simulations are able to account for the ionizing photons that are directly absorbed by the dust, we are only able to correct the H  $\alpha$  fluxes for reddening. According to Kim et al. (2019) a double-digit percentage might be lost this way. This cannot explain the difference to other observations, which have generally followed the same approach as we have, but it could help explain the higher values that we observe when compared to simulations.

## 4. Conclusion

We combine catalogues of H II regions with catalogues of young stellar associations and star clusters to measure the escape fraction across an unprecedentedly large sample of thousands of regions across 19 nearby galaxies. This dataset enables a statistical view of how much ionizing radiation escapes from the local H II region environment out into the galaxy disk.

To perform the calculation of  $f_{\text{esc}}$ , we compare  $Q_{\text{H}\alpha}$ , derived from the extinction-corrected H  $\alpha$  luminosity, and  $Q(H^0)$ , derived from the associated stellar counterpart. After comparing different methods of matching stars and gas, we focus our analysis on regions with a one-to-one match between a single H II region and a single stellar association. To mitigate the impact of stochastic sampling, we establish a robust subsample of 474 massive ( $> 10^4 M_{\odot}$ ) and young ( $\leq 8$  Myr) stellar associations that are fully contained in the nebula.

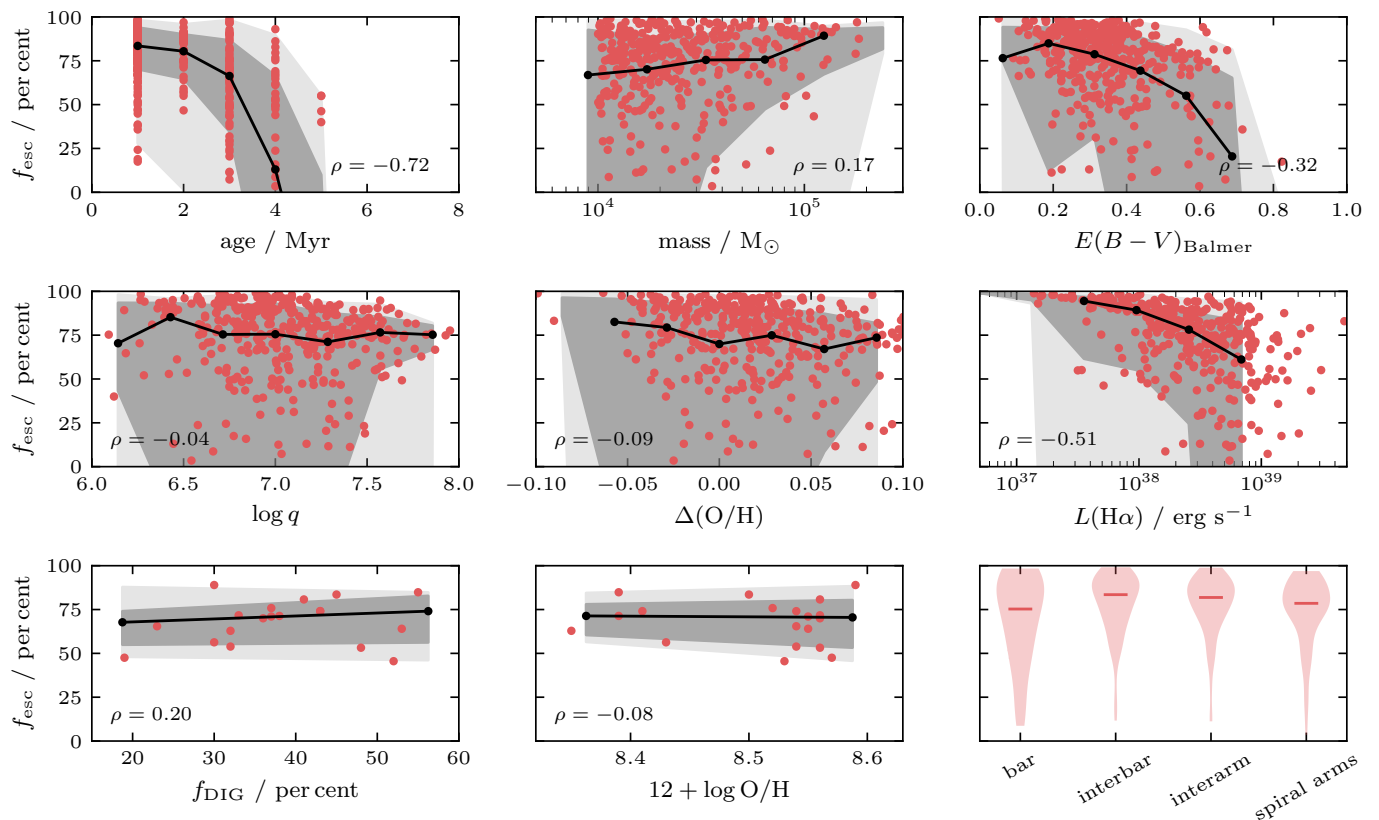


**Fig. 7.** Trends between different nebula properties and the escape fraction. Shown are the age and mass of the stellar associations, the reddening  $E(B - V)_{\text{Balmer}}$ , the ionization parameter  $\log q$ , the local metallicity offset  $\Delta(\text{O}/\text{H})$  of the  $\text{H II}$  region, and the luminosity  $L(\text{H}\alpha)$ . The last row shows the global escape fraction (see Section 3.4) versus the fraction of DIG emission, the global escape fraction versus the average metallicity of the galaxy, and the escape fraction for different environments. The black lines represent the median values in each bin and the gray shaded areas indicate the 68 and 98 percentiles.

- (i) From the robust one-to-one subsample, we measure a comparatively high value of  $f_{\text{esc}} = 82^{+12}_{-24}$  per cent.
- (ii) We derive similar escape fractions with different crossmatching methods or when using compact clusters instead of the loosely bound associations.
- (iii) The escape fraction depends heavily on the derived stellar parameters and the boundaries of the  $\text{H II}$  regions.
- (iv) For many  $\text{H II}$  regions, a significant fraction of the ionizing photon budget comes from stars that reside outside their boundaries.
- (v) If we take all stellar associations and  $\text{H II}$  regions together, to account for the entire ionizing photon budget in the galaxies, we measure slightly lower but consistent values.
- (vi) We do not identify any pronounced trends between  $f_{\text{esc}}$  and local or global galaxy properties.

This work demonstrates that a large fraction of ionizing photons can escape their immediate  $\text{H II}$  region bubble, and be available to power the surrounding pervasive DIG observed in local galaxies (Haffner et al. 2009; Belfiore et al. 2022).

Overall, more work is needed on precise determination of the stellar ionizing photon output before it is possible to establish more concrete connections between changes in  $f_{\text{esc}}$  and local conditions in the ISM.

We expect that significant progress on parametrising the properties of the stellar clusters will come from the inclusion of additional infrared *JWST* bands, and the use of priors based

on the presence of  $\text{H}\alpha$  emission (Whitmore et al. 2025). In addition, the recent availability of new *HST*  $\text{H}\alpha$  high resolution maps (Chandar et al. 2025) is enabling more detailed crossmatching between ionized gas and stellar populations at matched resolution for the brightest, most compact regions (Barnes et al. 2026). These maps already reveal the ways in which the clustering and hierarchical structuring of young stars make simple one-to-one matching of ionized gas and stars extremely challenging.

*Acknowledgements.* This work has been carried out as part of the PHANGS collaboration. Based on observations from the PHANGS-MUSE program, collected at the European Southern Observatory under ESO programmes 094.C-0623 (PI: Kreckel), 095.C-0473, 098.C-0484 (PI: Blanc), 1100.B-0651 (PHANGS-MUSE; PI: Schinnerer), as well as 094.B-0321 (MAGNUM; PI: Marconi), 099.B-0242, 0100.B-0116, 098.B-0551 (MAD; PI: Carollo) and 097.B-0640 (TIMER; PI: Gadotti). In addition, this research is based on observations made with the NASA/ESA Hubble Space Telescope obtained from the Space Telescope Science Institute, which is operated by the Association of Universities for Research in Astronomy, Inc., under NASA contract NAS 5-26555. Support for Program number 15654 was provided through a grant from the STScI under NASA contract NAS5-26555. FS and KK gratefully acknowledge funding from the Deutsche Forschungsgemeinschaft (DFG, German Research Foundation) in the form of an Emmy Noether Research Group (grant number KR4598/2-1, PI Kreckel) and the European Research Council’s starting grant ERC StG-101077573 “ISM-METALS”). MB acknowledges support from the ANID BASAL project FB210003. This work was supported by the French government through the France 2030 investment plan managed by the National Research Agency (ANR), as part of the Initiative of Excellence of Université Côte d’Azur under reference number ANR-15-IDEX-01. OE acknowledges funding from the Deutsche Forschungsgemeinschaft (DFG, German Research Foundation) – project-ID 541068876. SCOG and RSK acknowledge financial support from the European Research Council via the ERC Synergy Grant “ECOGAL” (project ID 855130) and from the German Excellence Strategy via the Heidelberg

Cluster of Excellence (EXC 2181 - 390900948) “STRUCTURES”. JEMD acknowledges support from project UNAM DGAPA-PAPIIT IG 101025, Mexico. MC and LR gratefully acknowledge funding from the DFG through an Emmy Noether Research Group (grant number CH2137/1-1). This research made use of *ASTROPY* (*Astropy Collaboration et al.* 2013, 2018, 2022), *NUMPY* (Harris et al. 2020), and *MATPLOTLIB* (Hunter 2007).

## References

- Adamo, A., Ryon, J. E., Messa, M., et al. 2017, *ApJ*, **841**, 131
- Anand, G. S., Lee, J. C., Van Dyk, S. D., et al. 2021, *MNRAS*, **501**, 3621
- Astropy Collaboration, Price-Whelan, A. M., Lim, P. L., et al. 2022, *ApJ*, **935**, 167
- Astropy Collaboration, Price-Whelan, A. M., Sipőcz, B. M., et al. 2018, *AJ*, **156**, 123
- Astropy Collaboration, Robitaille, T. P., Tollerud, E. J., et al. 2013, *A&A*, **558**, A33
- Bacon, R., Accardo, M., Adjali, L., et al. 2010, in Proc. SPIE, Vol. 7735, Ground-based and Airborne Instrumentation for Astronomy III, 773508
- Baldwin, J. A., Phillips, M. M., & Terlevich, R. 1981, *PASP*, **93**, 5
- Barnes, A. T., Chandar, R., Kreckel, K., et al. 2026, *A&A*, **706**, A95
- Barnes, A. T., Glover, S. C. O., Kreckel, K., et al. 2021, *MNRAS*, **508**, 5362
- Belfiore, F., Santoro, F., Groves, B., et al. 2022, *A&A*, **659**, A26
- Boquien, M., Burgarella, D., Roehly, Y., et al. 2019, *A&A*, **622**, A103
- Bruzual, G. & Charlot, S. 2003, *MNRAS*, **344**, 1000
- Cardelli, J. A., Clayton, G. C., & Mathis, J. S. 1989, *ApJ*, **345**, 245
- Cerviño, M. & Luridiana, V. 2006, *A&A*, **451**, 475
- Chabrier, G. 2003, *PASP*, **115**, 763
- Chandar, R., Barnes, A. T., Thilker, D. A., et al. 2025, *AJ*, **169**, 150
- Chisholm, J., Saldana-Lopez, A., Flury, S., et al. 2022, *MNRAS*, **517**, 5104
- Congiu, E., Blanc, G. A., Belfiore, F., et al. 2023, *A&A*, **672**, A148
- Crowther, P. A. 2007, *ARA&A*, **45**, 177
- da Silva, R. L., Fumagalli, M., & Krumholz, M. 2012, *ApJ*, **745**, 145
- da Silva, R. L., Fumagalli, M., & Krumholz, M. R. 2014, *MNRAS*, **444**, 3275
- Dale, J. E., Ercolano, B., & Bonnell, I. A. 2012, *MNRAS*, **424**, 377
- Dale, J. E., Ercolano, B., & Bonnell, I. A. 2013, *MNRAS*, **430**, 234
- Dayal, P. & Ferrara, A. 2018, *Phys. Rep.*, **780**, 1
- Della Bruna, L., Adamo, A., Lee, J. C., et al. 2021, *A&A*, **650**, A103
- Della Bruna, L., Adamo, A., McLeod, A. F., et al. 2022, *A&A*, **666**, A29
- Dolphin, A. E. 2000, *PASP*, **112**, 1383
- Doran, E. I., Crowther, P. A., de Koter, A., et al. 2013, *A&A*, **558**, A134
- Egorov, O. V., Lozinskaya, T. A., Moiseev, A. V., & Smirnov-Pinchukov, G. V. 2018, *MNRAS*, **478**, 3386
- Ekström, S., Georgy, C., Eggenberger, P., et al. 2012, *A&A*, **537**, A146
- Eldridge, J. J. & Stanway, E. R. 2009, *MNRAS*, **400**, 1019
- Eldridge, J. J., Stanway, E. R., Xiao, L., et al. 2017, *PASA*, **34**, e058
- Elmegreen, B. G. 2008, *ApJ*, **672**, 1006
- Emsellem, E., Schinnerer, E., Santoro, F., et al. 2022, *A&A*, **659**, A191
- Flury, S. R., Jaskot, A. E., Ferguson, H. C., et al. 2022a, *ApJS*, **260**, 1
- Flury, S. R., Jaskot, A. E., Ferguson, H. C., et al. 2022b, *ApJ*, **930**, 126
- Fouesneau, M. & Lançon, A. 2010, *A&A*, **521**, A22
- Fouesneau, M., Lançon, A., Chandar, R., & Whitmore, B. C. 2012, *ApJ*, **750**, 60
- Georgy, C., Ekström, S., Eggenberger, P., et al. 2013, *A&A*, **558**, A103
- Georgy, C., Ekström, S., Meynet, G., et al. 2012, *A&A*, **542**, A29
- Gerasimov, I. S., Egorov, O. V., Lozinskaya, T. A., Moiseev, A. V., & Oparin, D. V. 2022, *MNRAS*, **517**, 4968
- Gouliermis, D. A. 2018, *PASP*, **130**, 072001
- Grasha, K., Calzetti, D., Adamo, A., et al. 2015, *ApJ*, **815**, 93
- Groves, B., Kreckel, K., Santoro, F., et al. 2023, *MNRAS*, **520**, 4902
- Haffner, L. M., Dettmar, R. J., Beckman, J. E., et al. 2009, *Rev. Mod. Phys.*, **81**, 969
- Hanish, D. J., Oey, M. S., Rigby, J. R., de Mello, D. F., & Lee, J. C. 2010, *ApJ*, **725**, 2029
- Hannon, S., Lee, J. C., Whitmore, B. C., et al. 2019, *MNRAS*, **490**, 4648
- Hannon, S., Lee, J. C., Whitmore, B. C., et al. 2022, *MNRAS*, **512**, 1294
- Hannon, S., Whitmore, B. C., Lee, J. C., et al. 2023, *MNRAS*, **526**, 2991
- Harris, C. R., Millman, K. J., van der Walt, S. J., et al. 2020, *Nature*, **585**, 357
- Hassani, H., Rosolowsky, E., Koch, E. W., et al. 2024, *ApJS*, **271**, 2
- Hollyhead, K., Bastian, N., Adamo, A., et al. 2015, *MNRAS*, **449**, 1106
- Howard, C., Pudritz, R., & Klessen, R. 2017, *ApJ*, **834**, 40
- Howard, C. S., Pudritz, R. E., Harris, W. E., & Klessen, R. S. 2018, *MNRAS*, **475**, 3121
- Hummer, D. G. & Storey, P. J. 1987, *MNRAS*, **224**, 801
- Hunter, J. D. 2007, *Comput. Sci. Eng.*, **9**, 90
- Jacobs, B. A., Rizzi, L., Tully, R. B., et al. 2009, *AJ*, **138**, 332
- Japelj, J., Vanzella, E., Fontanot, F., et al. 2017, *MNRAS*, **468**, 389
- Kado-Fong, E., Kim, J.-G., Ostriker, E. C., & Kim, C.-G. 2020, *ApJ*, **897**, 143
- Kakiichi, K. & Gronke, M. 2021, *ApJ*, **908**, 30
- Kauffmann, G., Heckman, T. M., Tremonti, C., et al. 2003, *MNRAS*, **346**, 1055
- Kewley, L. J., Groves, B., Kauffmann, G., & Heckman, T. 2006, *MNRAS*, **372**, 961
- Kim, J., Chevance, M., Kruijssen, J. M. D., et al. 2021a, *MNRAS*, **504**, 487
- Kim, J.-G., Gong, M., Kim, C.-G., & Ostriker, E. C. 2023, *ApJS*, **264**, 10
- Kim, J.-G., Kim, W.-T., & Ostriker, E. C. 2019, *ApJ*, **883**, 102
- Kim, J.-G., Ostriker, E. C., & Filippova, N. 2021b, *ApJ*, **911**, 128
- Klessen, R. S. & Glover, S. C. O. 2016, *Saas-Fee Advanced Course*, **43**, 85
- Kreckel, K., Egorov, O. V., Belfiore, F., et al. 2022, *A&A*, **667**, A16
- Kreckel, K., Ho, I. T., Blanc, G. A., et al. 2020, *MNRAS*, **499**, 193
- Kroupa, P. 2001, *MNRAS*, **322**, 231
- Krumholz, M. R., Adamo, A., Fumagalli, M., et al. 2015, *ApJ*, **812**, 147
- Krumholz, M. R., McKee, C. F., & Bland-Hawthorn, J. 2019, *ARA&A*, **57**, 227
- Larson, K. L., Lee, J. C., Thilker, D. A., et al. 2023, *MNRAS*, **523**, 6061
- Lecroq, M., Charlot, S., Bressan, A., et al. 2024, *MNRAS*, **527**, 9480
- Lee, J. C., Sandstrom, K. M., Leroy, A. K., et al. 2023, *ApJ*, **944**, L17
- Lee, J. C., Whitmore, B. C., Thilker, D. A., et al. 2022, *ApJS*, **258**, 10
- Leitherer, C., Ekström, S., Meynet, G., et al. 2014, *ApJS*, **212**, 14
- Leitherer, C., Ortiz Otálvaro, P. A., Bresolin, F., et al. 2010, *ApJS*, **189**, 309
- Leitherer, C., Schaerer, D., Goldader, J. D., et al. 1999, *ApJS*, **123**, 3
- Lejeune, T., Cuisinier, F., & Buser, R. 1997, *A&AS*, **125**, 229
- Leroy, A. K., Hughes, A., Liu, D., et al. 2021a, *ApJS*, **255**, 19
- Leroy, A. K., Schinnerer, E., Hughes, A., et al. 2021b, *ApJS*, **257**, 43
- Levesque, E. M., Leitherer, C., Ekstrom, S., Meynet, G., & Schaerer, D. 2012, *ApJ*, **751**, 67
- Lopez, L. A., Krumholz, M. R., Bolatto, A. D., et al. 2014, *ApJ*, **795**, 121
- Ma, X., Quataert, E., Wetzell, A., et al. 2020, *MNRAS*, **498**, 2001
- Martin, D. C., Fanson, J., Schiminovich, D., et al. 2005, *ApJ*, **619**, L1
- Maschmann, D., Lee, J. C., Thilker, D. A., et al. 2024, *ApJS*, **273**, 14
- McLeod, A. F., Kruijssen, J. M. D., Weisz, D. R., et al. 2020, *ApJ*, **891**, 25
- Mitra, S., Ferrara, A., & Choudhury, T. R. 2013, *MNRAS*, **428**, L1
- Niederhofer, F., Hilker, M., Bastian, N., & Ercolano, B. 2016, *A&A*, **592**, A47
- O'Donnell, J. E. 1994, *ApJ*, **422**, 158
- Paardekooper, J. P., Pelupessy, F. I., Altay, G., & Kruijssen, C. J. H. 2011, *A&A*, **530**, A87
- Pellegrini, E. W., Oey, M. S., Winkler, P. F., et al. 2012, *ApJ*, **755**, 40
- Querejeta, M., Schinnerer, E., Meidt, S., et al. 2021, *A&A*, **656**, A133
- Rahner, D., Pellegrini, E. W., Glover, S. C. O., & Klessen, R. S. 2017, *MNRAS*, **470**, 4453
- Ramambason, L., Lebouteiller, V., Bik, A., et al. 2022, *A&A*, **667**, A35
- Ramambason, L., Schaerer, D., Stasińska, G., et al. 2020, *A&A*, **644**, A21
- Rousseau-Nepton, L., Martin, R. P., Robert, C., et al. 2019, *MNRAS*, **489**, 5530
- Rousseau-Nepton, L., Robert, C., Martin, R. P., Drissen, L., & Martin, T. 2018, *MNRAS*, **477**, 4152
- Saldana-Lopez, A., Schaerer, D., Chisholm, J., et al. 2022, *A&A*, **663**, A59
- Sana, H., de Mink, S. E., de Koter, A., et al. 2012, *Science*, **337**, 444
- Santoro, F., Kreckel, K., Belfiore, F., et al. 2022, *A&A*, **658**, A188
- Scheuermann, F., Kreckel, K., Barnes, A. T., et al. 2023, *MNRAS*, **522**, 2369
- Schlaflly, E. F. & Finkbeiner, D. P. 2011, *ApJ*, **737**, 103
- Simón-Díaz, S. & Stasińska, G. 2008, *MNRAS*, **389**, 1009
- Stetson, P. B. 1987, *PASP*, **99**, 191
- Storey, P. J. & Hummer, D. G. 1995, *MNRAS*, **272**, 41
- Tacchella, S., Smith, A., Kannan, R., et al. 2022, *MNRAS*, **513**, 2904
- Teh, J. W., Grasha, K., Krumholz, M. R., et al. 2023, *MNRAS*, **524**, 1191
- Thilker, D. A., Braun, R., & Walterbos, R. A. M. 2000, *AJ*, **120**, 3070
- Thilker, D. A., Lee, J. C., Whitmore, B. C., et al. 2025, *ApJS*, **280**, 1
- Thilker, D. A., Whitmore, B. C., Lee, J. C., et al. 2022, *MNRAS*, **509**, 4094
- Trebtsch, M., Blaizot, J., Rosdahl, J., Devriendt, J., & Slyz, A. 2017, *MNRAS*, **470**, 224
- Turner, J. A., Dale, D. A., Lee, J. C., et al. 2021, *MNRAS*, **502**, 1366
- Vázquez, G. A. & Leitherer, C. 2005, *ApJ*, **621**, 695
- Veilleux, S. & Osterbrock, D. E. 1987, *ApJS*, **63**, 295
- Wang, B., Heckman, T. M., Amorín, R., et al. 2021, *ApJ*, **916**, 3
- Wei, W., Huerta, E. A., Whitmore, B. C., et al. 2020, *MNRAS*, **493**, 3178
- Whitmore, B. C., Chandar, R., Lee, J. C., et al. 2025, *ApJ*, **982**, 50
- Zastrow, J., Oey, M. S., & Pellegrini, E. W. 2013, *ApJ*, **769**, 94
- Zurita, A., Rozas, M., & Beckman, J. E. 2000, *A&A*, **363**, 9

<sup>1</sup> Astronomisches Rechen-Institut, Zentrum für Astronomie der Universität Heidelberg, Mönchhofstraße 12-14, 69120 Heidelberg, Germany

<sup>2</sup> Universität Heidelberg, Zentrum für Astronomie, Institut für Theoretische Astrophysik, Albert-Ueberle-Str. 2, 69120, Heidelberg, Germany

<sup>3</sup> European Southern Observatory (ESO), Karl-Schwarzschild-Straße 2, 85748 Garching, Germany

<sup>4</sup> INAF – Osservatorio Astrofisico di Arcetri, Largo E. Fermi 5, I-50157 Firenze, Italy

- <sup>5</sup> International Centre for Radio Astronomy Research, University of Western Australia, 7 Fairway, Crawley, 6009 WA, Australia
- <sup>6</sup> Astronomy Australia Ltd. (Perth Office), University of Western Australia, 7 Fairway, Crawley, 6009 WA, Australia
- <sup>7</sup> Université Côte d’Azur, Observatoire de la Côte d’Azur, CNRS, Laboratoire Lagrange, 06000 Nice, France
- <sup>8</sup> Department of Physics & Astronomy, University of Wyoming, Laramie, WY 82071, USA
- <sup>9</sup> Research School of Astronomy and Astrophysics, Australian National University, Canberra, ACT 2611, Australia
- <sup>10</sup> Max Planck Institut für Astronomie, Königstuhl 17, 69117 Heidelberg, Germany
- <sup>11</sup> Universität Heidelberg, Interdisziplinäres Zentrum für Wissenschaftliches Rechnen, Im Neuenheimer Feld 225, 69120 Heidelberg, Germany
- <sup>12</sup> AURA for the European Space Agency (ESA), Space Telescope Science Institute, 3700 San Martin Drive, Baltimore, MD 21218, USA
- <sup>13</sup> Space Telescope Science Institute, 3700 San Martin Dr., Baltimore, MD 21218, USA
- <sup>14</sup> Department of Astronomy, The Ohio State University, Columbus, OH 43210, USA
- <sup>15</sup> Instituto de Astronomía, Universidad Nacional Autónoma de México, Ap. 70-264, 04510 CDMX, Mexico
- <sup>16</sup> Department of Astrophysical Sciences, Princeton University, 4 Ivy Lane, Princeton, NJ 08544, USA
- <sup>17</sup> Department of Physics, Tamkang University, No.151, Yingzhuang Road, Tamsui Dist., New Taipei City 251301, Taiwan
- <sup>18</sup> Department of Physics and Astronomy, The Johns Hopkins University, Baltimore, MD 21218, USA
- <sup>19</sup> Leiden Observatory, Leiden University, P.O. Box 9513, 2300 RA Leiden, The Netherlands
- <sup>20</sup> UK ALMA Regional Centre Node, Jodrell Bank Centre for Astrophysics, Department of Physics and Astronomy, The University of Manchester, Oxford Road, Manchester M13 9PL, UK

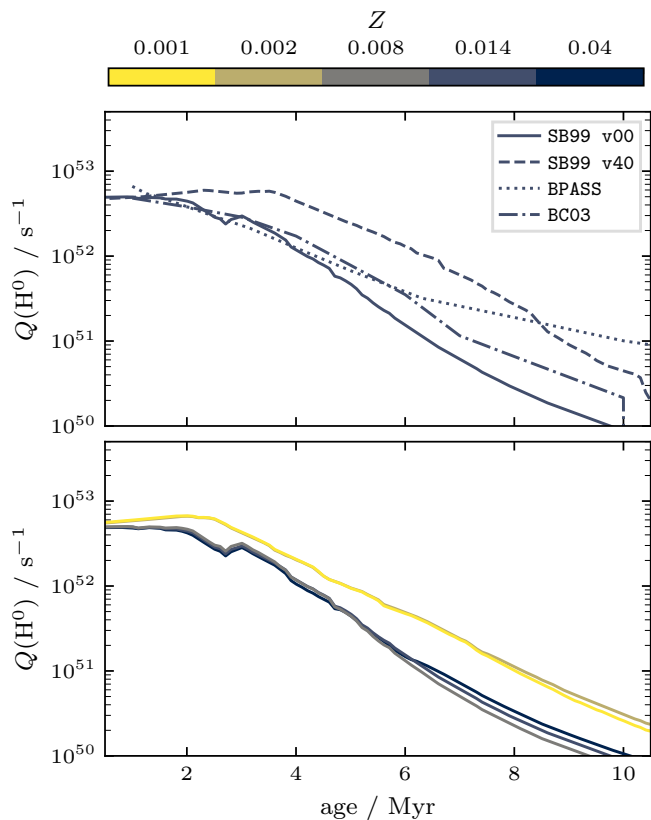


**Fig. A.1.** Ionizing photon flux  $Q(\text{H}^0)$  of a star cluster with a mass of  $10^6 M_\odot$  as a function of age. The top panel shows the values predicted by different models, all at solar metallicities, while the lower panel shows the SB99 v00 model at various metallicities.

## Appendix A: Ionizing photon flux from different models

In Figure A.1 we compare the ionizing photon flux  $Q(\text{H}^0)$  for different models (top panel) and metallicities (lower panel). A detailed listing of the models can be found in Table A.1. These plots demonstrate that, at constant metallicity, all models except the one with rotation are similar for the first few Myr. Around 6 Myr, however, the effects of binarity becomes relevant as its flux decreases much more slowly than the other models. For the impact of metallicity, we include the low-metallicity models from STARBURST99, based on the stellar model by Georgy et al. (2013). The variation between models that are close to solar metallicity is practically negligible, while the predicted flux is slightly higher at lower metallicities. Given that the flux decreases by an order of magnitude every few million years and the uncertainty of the age is comparatively high, the choice of model is likely to have only a minor influence.

## Appendix B: Comparison with Teh et al. (2023)

The stellar catalogues presented in Section 2.2 rely on the assumption that the clusters and associations in our sample are massive enough such that a deterministic relationship between the physical and photometric properties of the stellar populations exists. While we try to ensure this by focusing our analysis on high mass objects from the robust subsamples defined in Section 2.4, this means that we are omitting a large part of the sample. Another approach is to employ a stochastic stellar

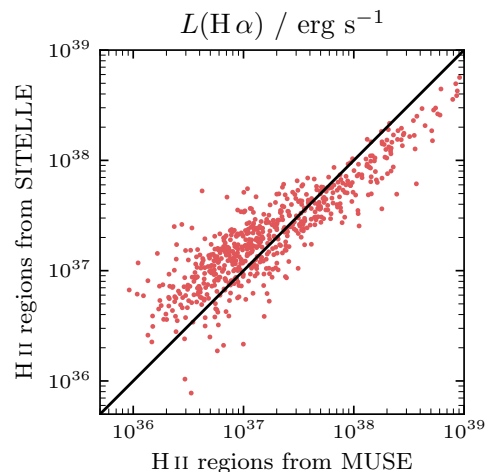


**Fig. B.1.** Comparisons between the H II regions from PHANGS (Groves et al. 2023, observed with MUSE) and the ones from SIGNALS (Rousseau-Nepton et al. 2019, observed with SITELLE).

population synthesis code like SLUG (da Silva et al. 2012, 2014) to infer a distribution of possible values for  $Q(\text{H}^0)$ .

A particularly relevant literature result is the study by Teh et al. (2023), who measured the escape fraction of NGC 0628 (which is also in our sample) with the help of SLUG. They combined H II regions from the Star formation, ionized gas and nebular abundances legacy (SIGNALS) survey (Rousseau-Nepton et al. 2018) with star clusters from LEGUS (Grasha et al. 2015; Adamo et al. 2017). A large fraction of the 139 objects in their matched catalogue have negative escape fractions and based on a subsample of 42 objects, they measured a comparatively low value of  $f_{\text{esc}} = 9 \pm 6$  per cent. The striking difference to our results asks for a closer comparison.

We start by comparing the H II regions from MUSE to those from SITELLE and 643 of them match within 0.8 arcsec. In Figure B.1 we compare the measured fluxes, and while the ones identified by SIGNALS are more luminous at the fainter end, the ones from PHANGS are brighter for the most luminous objects.

To compare the stellar component, we take the five-band filters from our association catalogue and redo the SED fit with SLUG, following the procedure described in Teh et al. (2023): First, a library of  $10^7$  stellar populations is generated to account for the effects of stochasticity in the IMF. For this, we adopt the following physical parameters: Solar metallicity, the IMF by Kroupa (2001), Geneva evolutionary tracks (Ekström et al. 2012; Georgy et al. 2012), STARBURST99 stellar atmosphere models (Leitherer et al. 1999; Vázquez & Leitherer 2005), and a Milky Way extinction curve (Cardelli et al. 1989). Then we use a modified version of cluster\_slug (Della Bruna et al. 2021, 2022; Teh et al. 2023) to compute the posterior probability density function (PDF) of the age, mass, and ionizing luminosity (see Krumholz et al. 2015, for more details). We represent the  $Q(\text{H}^0)$  values with the median (50th percentile) and the  $1\sigma$  uncertainty with the 16th–84th percentile of the PDF distribution.

The result is shown in Figure B.2. As far as the masses are concerned, there is a large scatter, but not systematic differences. There are significant deviations in the derived ages, with those from SLUG generally being older. This is particularly problematic in the case of very young stars. While the lower limit of the age distribution is often consistent with being 3 Myr or younger, the median rarely is. Since the majority of the ionizing photons

**Table A.1.** Codes used to compute the ionizing photon flux  $Q(\text{H}^0)$ .

Name	Code	Stellar model	IMF
BC03	CIGALE (Boquien et al. 2019)	BC03 (Bruzual & Charlot 2003)	(Chabrier 2003)
SB99 v00	STARBURST99 (Leitherer et al. 2014)	Geneva without rotation (Ekström et al. 2012)	(Kroupa 2001)
SB99 v40	STARBURST99 (Leitherer et al. 2014)	Geneva with rotation (Ekström et al. 2012)	(Kroupa 2001)
BPASS	BPASS (Eldridge & Stanway 2009)		(Kroupa 2001)
SLUG	SLUG (da Silva et al. 2012)	Geneva (Ekström et al. 2012)	(Kroupa 2001)

are emitted during this period, the predicted fluxes are generally lower.

When matched to the H II region catalogue from MUSE, we can compute the resulting escape fractions as shown in [Figure B.3](#). Only 776 of them ( $\sim 19$  per cent) have positive escape fractions, and their escape fractions are uniformly distributed across the entire range from 0 to 100 per cent. If we focus on the young, massive, and contained objects that form a robust subsample, we find 228 objects that fulfil our criteria and only 50 of them ( $\sim 22$  per cent) have positive escape fractions. It was to be expected that SLUG would deliver different values at the faint end, due to stochastic sampling. Overall, it predicts systematically lower  $Q(\text{H}^0)$ , even at the bright end, where stochastic sampling should not be an issue. The lower  $Q(\text{H}^0)$  is responsible for significantly lower escape fractions, which are mostly uniformly distributed between 0 to 45 per cent, and are in better agreement with results found by previous studies that are based on SLUG ([Della Bruna et al. 2022](#); [Teh et al. 2023](#)).

### Appendix C: Completeness issues

In [Section 3.4](#) we consider the entire ionizing photon budget of each galaxy. In this scenario, different completeness limits for the H II regions and stellar populations could bias those results. We therefore estimate the completeness for both to assess the contribution of missed objects. In [Figure C.1](#) we show the normalised cumulative ionizing photon flux to estimate the contribution of faint H II regions and low-mass associations.

In the case of IC 5332, NGC 3351 and NGC 5068, faint H II regions (below the completeness limit from [Santoro et al. 2022](#)) contribute more than 10 per cent of the total ionizing photon flux. The potentially missing H  $\alpha$  flux could increase the escape fraction, but while the values of the first two galaxies are above the average (see [Table 3](#)), both also appear on the stellar side, weakening this conclusion.

For IC 5332, NGC 1300, NGC 1433, NGC 1512, NGC 2835 and NGC 3351, the contribution of low-mass associations ( $< 5000 M_{\odot}$ ) is larger than 10 per cent. In contrast to the case of the H II regions, the potentially overlooked clusters would lead to a decrease of the escape fraction. While half of galaxies have lower escape fractions, the other half, including the two galaxies mentioned above, have higher values.

For the 12 other galaxies, the completeness limit should not be an issue, and even for the seven discussed above, there is no noticeable impact.

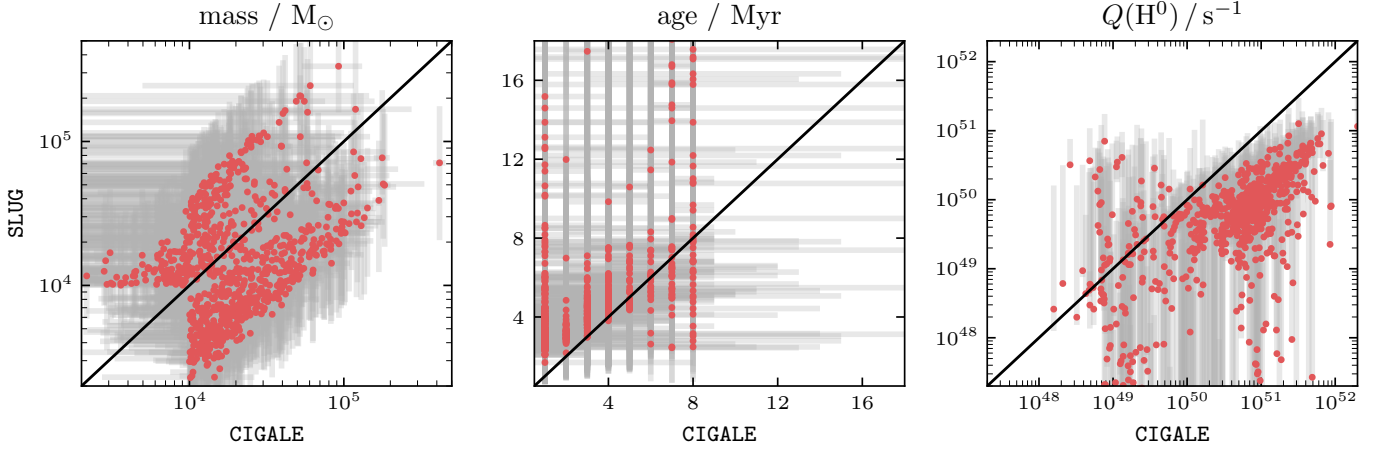


**Fig. B.2.** We ran SLUG on the stellar associations in the matched catalogue. For the comparison we define a robust subsample, where either CIGALE or SLUG predict an age younger than 8 Myr and a mass above  $10^4 M_{\odot}$  (859 objects). The masses show a wide scatter in both directions, but SLUG generally predicts older ages. As a result, the ionizing photon flux is systematically lower than the one from CIGALE.

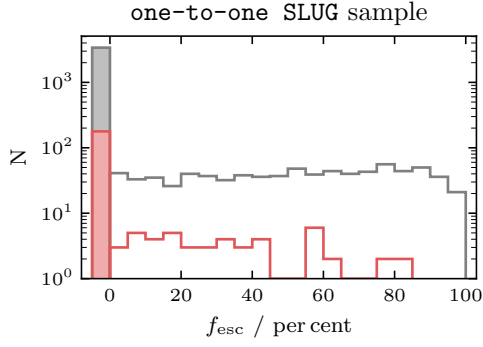


**Fig. B.3.** Histograms of the escape fractions based on stellar parameters inferred from SLUG. The full sample is shown in gray and the robust subsample of young and massive, fully contained associations is shown in red. All regions with negative escape fractions are grouped together in the shaded left bar.

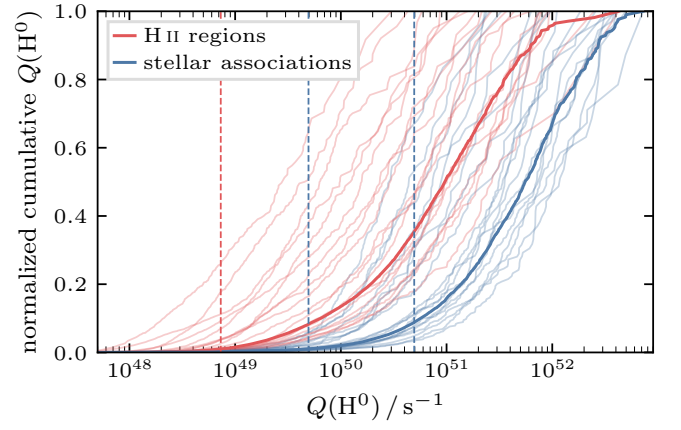


**Fig. C.1.** Normalized cumulative  $Q(H^0)$  as a function of  $Q(H^0)$  for H II regions and stellar associations. The individual galaxies are shown in pastel and the sum of all galaxies is shown in bold colours. We only show the H II regions and associations in the overlapping coverage that do not fall in the centre (corresponding to the sample used in Section 3.4). The H II region completeness limit from Santoro et al. (2022), corresponding to a luminosity of  $10^{37}$  erg  $s^{-1}$  is indicated by the left red dashed line. The two blue lines corresponds to a  $10^3 M_{\odot}$  and  $10^4 M_{\odot}$  cluster that is 1 Myr old.